Three-Phase PV Pumping System with Advanced Control for Enhanced Efficiency and Robustness: Modeling, Experimental Validation and Optimisation

Marwen Bjaoui [a,*], Benoît Larroque [a], Ridha Djebali [b,*],Lotfi khemissi [c], Robert Ruscassié [d], Ridha Benadli [e], Franck Luthon [a], Anis Sellami [f]

[a] Université de Pau et des Pays de l'Adour, E2S UPPA, SIAME, EA4581, 64600, Anglet, France
[b] UR22ES12: Modeling, Optimization and Augmented Engineering, ISLAIB, University of Jendouba, Béja 9000, Tunisia
[c] Laboratory of Nanomaterials and Systems for Energy (LaNSER), Research and Technology Centre of Energy (CRTEn), Borj Cedria, Tunisia
[d] Laboratory for Applied Mechanical and Electrical Engineering Sciences—IPRA Federation, University of Pau et des Pays de l'Adour/E2S UPPA, 64000 Pau, France.
[e] IREENA Laboratory, University of Nantes, 44600 Saint-Nazaire, France
[f] Research unit: LISIER, National Higher Engineering School of Tunis, Tunis 2050, Tunisia
[*] Corresponding author: bjaouimarwen@yahoo.fr, ridha.djebali@islaib.u-jendouba.tn

Abstract

This paper presents a detailed study of a three-phase photovoltaic pumping system (PVPS), comprising a 1.5 kW three-phase induction motor for water pumping, a three-phase voltage source inverter (VSI), and a DC-DC boost converter designed to maximize power extraction from a 1.88 kWp photovoltaic generator (PVG). The system is characterized by its cost-effectiveness, high efficiency, and robust performance. To reduce overall system costs, the inductor current of the boost converter and the rotational speed of the induction motor are estimated rather than measured directly. A nonlinear neural network observer (NNO) is employed to estimate the inductor current, while a sliding mode observer (SMO) is utilized to estimate the motor speed. To enhance the system's resilience against internal and external disturbances, a hybrid incremental conductance super-twisting sliding mode controller (InC-STSMC) is implemented for maximum power point tracking (MPPT) from the PVG, and a flux-oriented sliding mode vector control (FO-SMC) is adopted for precise regulation of the motor speed. The effectiveness of the proposed control strategy is evaluated through model-in-the-loop (MIL) simulations conducted in the MATLAB-Simulink environment, demonstrating significant improvements in dynamic performance, particularly in terms of stability and robustness, compared to conventional proportional-integral (PI) control methods. The practicality and suitability of the proposed InC-STSMC combined with the NNO scheme are further validated through a processor-in-the-loop (PIL) test using the STM32F769I board, highlighting its potential for real-world applications.

Keywords: Photovoltaics; maximum power point tracking; water pumping; sliding mode control; observers, STM32F769I.

1. Introduction

Water pumping systems (WPS) are generally categorized into two types: direct current (DC) and alternating current (AC) systems. In regions where AC power is readily available from the local electrical grid, AC-powered WPS are often more cost-effective and require less maintenance [1]. However, in many rural areas, water sources are distributed across large distances, creating significant operational challenges.

Traditionally, two primary solutions have been employed to power WPS in remote areas: the construction of new power lines to transport electricity over long distances or the use of localized diesel generators. The first approach is often prohibitively expensive due to the high costs associated with installing power lines and transformers. The second approach, while appearing simpler, presents several challenges, including issues related to fuel availability, transportation, maintenance, and the high costs of diesel fuel in rural regions [2-4].

In recent years, renewable energy has emerged as a viable and sustainable solution for farmers in isolated areas with limited access to conventional fuel and electricity. Renewable energy sources have been increasingly applied to activities such as irrigation and rural electrification, helping residents meet their needs for fresh water and agricultural productivity. Furthermore, these solutions improve the quality of life in rural communities and drive socio-economic development. In this context, PVPS have been highlighted as effective technology to address critical drinking water and irrigation requirements in remote agricultural areas, as described by the authors in [5].

The primary objective of a PVPS is to maximize the volume of water pumped while operating under a variable energy source that is highly dependent on environmental factors such as temperature and solar radiation [6].

To address this challenge, various PVPS configurations have been explored and proposed in the literature. These configurations are generally classified into two main categories: PVPS with energy storage and direct-connected PVPS.

In [7], the performance of a PVPS with battery storage was analyzed. Two MPPT algorithms—perturb and observe (PO) and fuzzy logic control (FLC)—were implemented and compared to optimize system efficiency. The study concluded that the FLC algorithm outperformed the PO algorithm in terms of both response speed and system stability. Similarly, in [8], the authors investigated PV-battery-powered systems and developed an evaluation framework for secondary applications such as water pumping. Their primary objective was to meet an energy demand of 3.2 kWh/day for rural housing units. The study demonstrated that the sizing of PV battery systems is dependent on the number of PV panels and the battery capacity, which can be adjusted to meet specific energy requirements.

Other PVPS configurations with energy storage integrate PV panels with additional renewable energy sources and storage technologies to create hybrid pumping systems, such as PV/Wind/Battery, PV/Wind/Battery/Diesel, and PV/Battery/Supercapacitor systems. Notably, supercapacitors provide the advantage of rapid dynamic power regulation, which reduces the frequency of charge-discharge cycles. However, their inclusion significantly increases the overall cost of the system [9-11]. Among the various PVPS configurations with energy storage, lead-acid battery systems remain the most widely adopted option due to their low cost and high availability.

The most common configuration for PVPS currently involves coupling the motor pump system directly to the PVG via a power electronic interface, without incorporating energy storage [12]. In this arrangement, the overall cost of the system is reduced by substituting electrochemical storage with a water storage tank. A two-stage PVPS utilizing an induction motor (IM) is described in [3]. In this system, scalar control (V/f) is employed to regulate the speed of the IM, while a DC-DC boost converter in the first stage is controlled by an incremental conductance (InC) algorithm to extract maximum power from the photovoltaic generator.

A similar configuration, comprising a photovoltaic array, a DC-DC boost converter, an inverter, and an induction motor (IM) driving a centrifugal pump, is simulated in [13]. In this study, the authors implemented a variable step-size perturb and observe (PO) MPPT controller to optimize power extraction from the PVG. Additionally, they proposed a fuzzy logic control (FLC) technique to improve the performance of conventional direct torque control (DTC) for the IM.

Furthermore, single-stage PVPS configurations employing a single-power electronic interface have been widely investigated in the literature [14]. In these systems, the PVG is directly connected to the IM, which drives a centrifugal pump via single-phase or three-phase inverters. These inverters are configured to extract the maximum available power from the PVG, offering a simpler and potentially more cost-effective solution compared to multi-stage configurations.

In response to advancements in PV systems, research efforts have increasingly focused on sophisticated control methodologies, particularly nonlinear strategies, to optimize system performance and enhance robustness under dynamic operating conditions. Sliding mode control (SMC) has emerged as a prominent technique due to its demonstrated effectiveness and inherent resilience in such environments [15]. Comparative studies have indicated that SMC exhibits superior performance in motor speed control compared to fuzzy logic controllers (FLC) and proportional-integral-derivative (PID) regulators [16]. Furthermore, its capacity to maintain optimal performance despite variations in environmental conditions renders it a suitable solution for maximizing energy efficiency and ensuring the reliability of PV water pumping systems [17]. This motivates our investigation into a robust and efficient MPPT strategy tailored for PV applications.

For DC-DC converters, diverse sliding surface designs have been proposed. For instance, the SMC approach detailed in [18] necessitates the measurement of capacitor current, load current, and output voltage, while alternative techniques [19, 20] rely on inductor current, input voltage, and output voltage measurements. The selection of appropriate state variables is paramount for effective DC-DC converter control. Literature suggests that efficient regulation can be achieved by monitoring either the inductor current and output voltage or the input voltage [21, 22]. Specifically, [22] proposes a control algorithm based on output voltage and inductor current measurements, whereas [21] advocates for an approach utilizing input voltage and inductor current measurements.

Complementing these measurement strategies, the choice of control technique is critical for ensuring system stability and overall performance. In this regard, advanced nonlinear control methods, such as SMC, and adaptive strategies, including PI controllers augmented with observers, have been extensively explored.

Among advanced control techniques, SMC is particularly notable for its inherent robustness to load and input voltage variations. This robustness is achieved by imposing system dynamics that constrain the state trajectory to a predefined sliding surface. The inclusion of an integral term in the sliding surface further enhances steady-state accuracy by eliminating steady-state errors [23]. However, a significant drawback of SMC is the occurrence of chattering, an undesirable high-frequency oscillatory phenomenon that can adversely affect the longevity of system components. To mitigate this issue, advanced techniques such as the Super-Twisting Algorithm (STA) have been developed, which effectively reduce chattering and ensure smoother convergence toward the sliding surface [24-26].

In comparison, the Proportional-Integral (PI) controller augmented with an observer offers an alternative approach by estimating unmeasured states and disturbances in real time. This capability enables adaptive control adjustments in response to system variations, resulting in smoother responses and reduced overshoot compared to classical control methods [27]. However, the performance of PI controllers with observers is highly dependent on the accuracy of the observer and the quality of the system model used for state and disturbance estimation [28]. While these controllers demonstrate effective disturbance rejection, they tend to adapt more slowly to rapid changes in operating conditions, as evidenced in [29]. Experimental results indicate that such controllers can achieve successful reference tracking, with voltage tracking errors converging to zero within 56 ms after a transient and 50 ms following a step change in the reference voltage. Nonetheless, when compared to SMC-based strategies [30], PI controllers with observers generally exhibit slower responses to dynamic variations, highlighting a trade-off between smoothness and adaptability.

Building on these foundational control techniques, recent research has increasingly focused on hybrid and intelligent control strategies to achieve enhanced performance. In [31], a STSMC integrated with an artificial neural network (ANN) is proposed for maximizing power extraction in photovoltaic (PV) systems. The STSMC regulates a boost converter, while the ANN dynamically generates the MPPT voltage reference, enabling sensorless MPPT operation. The sliding surface is defined based on the error between the PV generator's output voltage and its reference, as well as the inductor current and the output voltage of the DC-DC converter. This combined approach ensures real-time adaptation to environmental variations, such as changes in irradiance and temperature, leading to high efficiency and robust performance. The system is evaluated through MATLAB/Simulink simulations, demonstrating an MPPT convergence time of less than 2.5 ms with minimal oscillations around the maximum power point (MPP). The study focuses on PV DC systems with resistive loads, utilizing a DC-DC buck-boost converter to improve power transfer efficiency.

Similarly, [32] proposes a hybrid control strategy that combines STSMC with a self-evolving recurrent Chebyshev fuzzy neural network (SERCFNN) for precise voltage regulation in a DC-DC buck converter. The STSMC is employed to mitigate the chattering phenomenon, while the SERCFNN estimates system nonlinearities, thereby enhancing overall control performance. The sliding surface is defined based on the error between the DC-DC converter's output voltage and its reference, along with the derivative of this error. This approach ensures high robustness against disturbances and achieves low tracking error. The system is implemented on a DS1104 DSP controller, demonstrating an output voltage response time of less than 60 ms and a near-zero tracking error of just 0.08 V. This study is particularly relevant for applications requiring stable voltage regulation, such as systems with resistive loads, and validates the control strategy on a DC-DC buck converter, ensuring efficient and reliable operation.

In the context of DC-DC boost converters, the inductor current exhibits high-frequency characteristics, necessitating the use of sensors with wide bandwidth capabilities. The most widely adopted method for measuring inductor current involves the combination of a shunt resistor and a high-side current sensing amplifier [33]. This approach is particularly recommended for boost converters due to the high-frequency nature of the inductor current, as emphasized in [34] and [35]. While this method is relatively straightforward to implement, it is associated with significant power losses attributable to the sensing resistor. A comprehensive review of current sensing techniques is provided in [36], which discusses their respective advantages and limitations.

Similarly, in induction motor control, speed sensors such as tachometers, resolvers, or digital encoders are frequently employed to provide speed feedback. However, the integration of these sensors increases system costs and can compromise reliability due to their physical space requirements and vulnerability to environmental degradation [37].

Given the aforementioned drawbacks, the elimination of physical sensors offers a dual benefit: reducing hardware costs and simplifying the control architecture of PV systems. To address the challenges associated with measuring inductor current and IM speeds such as increased costs and added hardware complexity—various estimation algorithms have been developed. These algorithms provide a viable alternative to physical sensors, enhancing system efficiency and reliability while mitigating the limitations of traditional sensing methods.

In [38], the authors proposed a Luenberger observer to estimate the inductor current in a boost converter for PV systems. The estimated current is utilized in a PO-based MPPT algorithm. While this approach is cost-effective, reduces system complexity, and is commended for its simplicity and reliability in steady-state conditions, it exhibits sensitivity to model inaccuracies. These inaccuracies can lead to poor estimation or instability, particularly in highly nonlinear or fast-dynamic systems—critical challenges for DC-DC converters.

In [39], the authors propose the use of an Extended Kalman Filter (EKF) for inductor current estimation in a DC-DC boost converter. Although the EKF is well-suited for nonlinear and noisy systems, its application to DC-DC boost converters faces specific challenges. A key issue is the variability of the load value, a critical parameter in EKF design, which changes with operating conditions. This variability can introduce errors in current estimation and compromise the accuracy of output voltage filtering. Similarly, reference [30] introduces a high-gain observer (HGO) for inductor current estimation in a PV storage system. While simulation results demonstrate the effectiveness of the HGO, experimental validation reveals limited performance, with significant estimation errors.

The method proposed in [40] employs a state observer based on Lyapunov’s direct method to estimate the inductor current in a power converter. This approach integrates a PI controller for reference current generation with a nonlinear control strategy for output voltage regulation. Although this method improves performance by reducing the mean squared error (MSE) by 27% and peak overshoot by 34% during load variations, it exhibits a persistent overshoot during voltage reference changes, representing a notable limitation.

To address external disturbances and parameter uncertainties, reference [41] proposes a high-order sliding mode disturbance observer (HOSMDO) for estimating lumped disturbances in a buck/boost converter. This approach effectively mitigates unmatched disturbances caused by input voltage fluctuations, load variations, output voltage regulation, power flow changes, and model uncertainties. Additionally, it enables the observation of inductor current, eliminating the need for a current sensor and thereby reducing system cost and complexity. However, the method is not without limitations, as load power variations induce a 2.5 V overshoot in the output voltage, which can destabilize the sliding surface.

This research investigates a simulated PVPS in MATLAB-Simulink, consisting of a 1.88 kWp PVG, a boost converter, a 1.5 kW IM, and a centrifugal pump. A new method is introduced to optimize the PVPS's cost, efficiency, and response time. To lower expenses, the system eliminates the inductor current sensor and IM speed sensor by using neural network observers (NNO) and sliding mode observers, respectively. A hybrid control strategy is implemented to improve the PVPS's efficiency and resilience against internal and external disturbances. This strategy combines InC-STSMC for MPPT with FO-SMC for IM speed regulation. This control approach ensures the PVPS operates stably despite changing weather conditions and internal parameter uncertainties. The estimated inductor current is incorporated into the control law to improve the STSMC’s performance. This optimizes MPPT and ensures accurate DC bus voltage regulation with minimal oscillations, thus enhancing overall system stability. Furthermore, the NNO continuously adapts to real-time variations, mitigating the impact of measurement noise and sensor limitations, which further strengthens the robustness and reliability of the proposed control strategy.

The structure of this paper is organized as follows: Section 2 presents the mathematical model of the proposed PVPS, providing a detailed description of the system architecture. Section 3 outlines the proposed control strategy. Section 4 discusses simulation results, while Section 5 presents the experimental validation. Finally, Section 6 concludes the paper.

2. Mathematical Modeling of the PVPS

The proposed structure of the photovoltaic (PV) water pumping system is illustrated in Fig. 1. The system consists of a 1.5 kW induction motor (IM) driven by a 1.88 kWp photovoltaic generator (PVG), connected to a centrifugal pump through a three-phase voltage source inverter (VSI) and a DC-DC boost converter. The boost converter is controlled using an incremental conductance/super-twisting sliding mode control (InC-STSMC) to maximize power extraction from the PVG. The IM is regulated by a fractional-order sliding mode control (FO-SMC) to enhance its stability and robustness [42-43]. To reduce system costs, the inductor current sensor and IM speed sensor are eliminated and replaced by a neural network observer (NNO) and either a Luenberger observer (LO) or a sliding mode observer (SMO), respectively.

2.1. Modeling and design of the PVG

A PVG generates a photovoltaic (PV) current proportional to the irradiation [30]. A PVG is an association of N_p parallel branches of N_s series PV modules. Its mathematical model can be written as:

$$I_{pv} = N_p I_{pv} - N_p I_s \left[exp\left(\frac{q}{k.T.A} \left(\frac{V_{pv}}{N_s} + \frac{I_{pv} R_s}{N_p} \right) - 1 \right) \right] - \frac{N_p V_{pv} + N_s I_{pv} R_s}{N_s R_s} \tag{1}$$

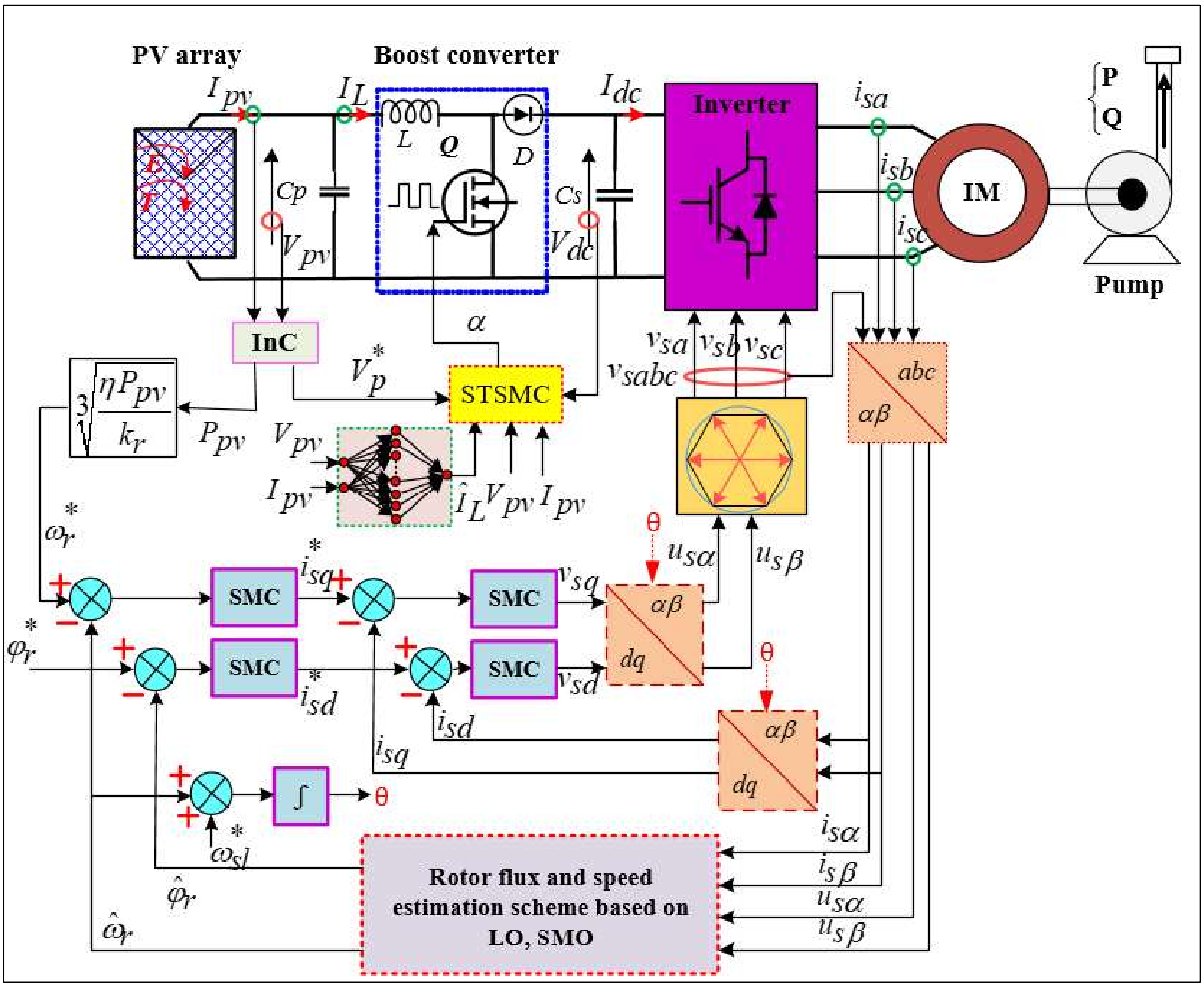

Fig. 1 PVPS power stage and control system.

The PV panel parameters used in this paper are summarized in Table 1.

The required power of the PVG can be calculated as [44]:

$$P_{pv} = \frac{1.2\ K_H\ Q\ H_{mt}}{t_h\ \eta_{pm}} \tag{2}$$

where K_H is the hydraulic constant; Q is the flow rate (m^3/Hours); H_{mt} is the manometric head (m); t_h is the pumping operating time (hours), and η_{pm} is the motor-pump efficiency (%). Power losses in cables and power converters are estimated at 20 % [3].

Table 1 Electrical parameters of the PV module

PV parameters	Variable	Values
Maximum power	P_{mp}	235.024 Watts

Voltage at MPP	V_{mp}	29.6 V
Current at MPP	I_{mp}	7.94 A
Open circuit voltage	V_{OC}	36.8 V
Short circuit current	I_{SC}	8.54 A
number of cells	N_s	60

The PVG power is designed to operate for 6.6 hours/day with a flow rate of 80.2 m^3/day. The water tank is located at 20 m. Considering a motor pump efficiency of 45 %, the PVG power is selected to 1.88 kWp. The PVG is composed of one branch of 8 PV modules in series (Ns = 8 and Np = 1). The induction machine driving the pump has a power of 1.5 kW [**45**].

The PVG is simulated using Matlab-Simulink software, Fig. 2 and Fig. 3 illustrate their P-V and I-V characteristics, respectively.

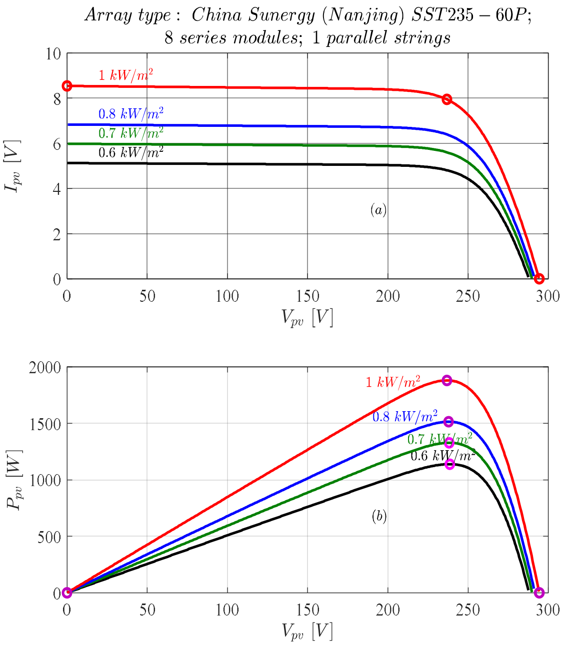

Fig. 2 PVG characteristics under variable irradiation:(a) PV Current versus PV voltage (b) PV power versus PV voltage

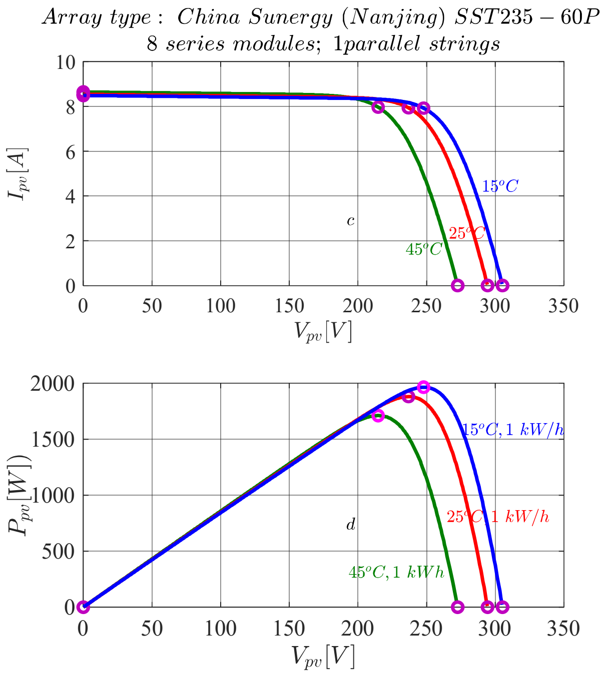

Fig. 3 PVG characteristics under variable temperature:(a) PV power versus PV voltage (b) PV current versus PV voltage

2.2. Modeling and design of the DC-DC boost converter

In continuous mode operation, the boost converter is designed. The inductor L and the output capacitor C_s can be calculated as follows [46-48]:

$$L = \frac{V_{mp}\,\alpha}{\Delta\, I_{mp}\ \ f_s} = \frac{V_{mp}\left(V_{dc} - V_{mp}\right)}{\Delta I_L\, f_s\, V_{dc}} \tag{3}$$

$$C_s = \frac{I_{dc}\,(1-\alpha)}{\Delta V_{dc}\, f_s} \tag{4}$$

where, f_s is fixed to 10 kHz, $\Delta \mathrm{I_L}$ is fixed to 20% of $\mathrm{I_{mp}}$, α is the duty cycle of the boost converter, $\mathrm{V_{dc}}$ is fixed to 650 V with a maximum ripple of 2% and I_{dc} is the maximum current motor phase. This yields to select $L = 3\ mH$ and $C_s = 110\ \mu\mathrm{F}$.

The DC-DC boost converter's dynamic behavior is provided by [49]:

$$\begin{cases} \dfrac{dV_{pv}}{dt} = \dfrac{1}{C_p}\left(I_{pv} - I_L\right) \\ \dfrac{dI_L}{dt} = \dfrac{1}{L}\left(V_{pv} - (1-\alpha)V_{dc}\right) \end{cases} \tag{5}$$

***2.3.** Model and design of the VSI*

The DC bus voltage is converted to an AC voltage using a three-phase VSI to feed the IM. To size the VSI, an estimation of the nominal values of voltage and current is required. The required voltage and current of an IGBT switch are calculated as [47-48, 50]:

$$V_{VSI} = 1.4\, V_{dc} = 910\ \mathrm{V} \tag{6}$$

$$I_{VSI} = 1.2\, I_{dc} = 2.64\ \mathrm{A} \tag{7}$$

Where 1.4 and 1.2 are safety factors to accommodate switching transients. Finally, the required VA power of VSI is estimated as follows:

$$S_{VSI} = V_{VSI} \times I_{VSI} \simeq 2.5\ \text{kVA} \tag{8}$$

SVPWM controls the three-phase inverter, one of the most popular methods to generate sinusoidal voltage and current with high efficiency and low harmonic distortion. The main idea of the SVPWM control technique is to create six sectors —1, 2, 3, 4, 5 and 6—out of the 2D plane. Then, the required output voltage is therefore represented by an equivalent vector, V_{ref}, which rotates counterclockwise, as seen in Fig. 4. We can transition from the three-dimensional plane to the two-dimensional plane using the Clarke (αβ) transformation. The ABC-αβ transformation yields component vectors for every fundamental switching vector, as shown in Fig. 4.

As shown in Fig.4, eight possible vectors can be represented in the space vector.

$$\vec{V}_k = \frac{2}{3} V_{dc}\, exp\left(\frac{j(k-1)\pi}{3}\right), k = 1 - 6 \tag{9}$$

The three vectors that are closest to the sector the reference voltage V_{ref} is in make up its composition, and it can be in any sector. An illustration of a specified reference voltage on sector (**1**) with angular frequency is shown in Fig. 5. It uses three vectors (V_1, V_0, V_2) to close this sector.

To generate 3-phase inverter switching signals, the following steps need to be used:

a. The angle δ is obtained and the sector to which V_{ref} belongs is identified using the voltages V_α, V_β and V_{ref}.

b. The switching times T_0,T_1 and T_2 in all sectors are calculated by the following equations [**51**]:

$$\begin{cases} T_1 = m\frac{\sqrt{3}}{\pi} T_s sin\left(\frac{\pi}{3} - \delta\right) \\ T_2 = m\frac{\sqrt{3}}{\pi} T_s sin(\delta) \\ T_0 = \frac{T_s}{2} - (T_1 + T_2) \end{cases} \quad \text{where } k = 1 - 6, m = \left|\frac{V_{ref}}{\frac{2}{3} V_{dc}}\right|, T_s = \frac{1}{f_s}, 0 \le \delta \le \frac{\pi}{3} \tag{10}$$

c. Switching signals are generated for the determined switching sequences based on the determined times.

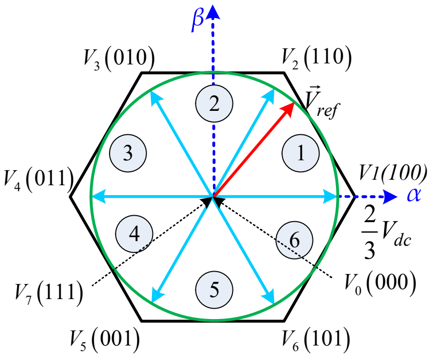

Fig. 4 SVPWM vectors sequence.

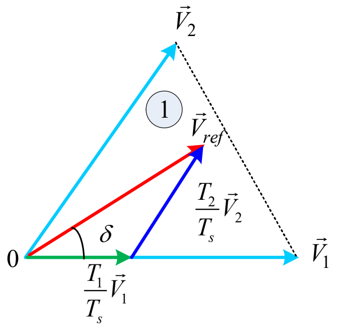

Fig. 5 Sectors (1) vectors.

2.4. Modeling of the IM

In the (α − β) frame, the state space model of the IM can be expressed as follows, [52]:

$$\begin{cases} \dot{X} = EX + WU \\ Y = MX \end{cases} \tag{11}$$

where: $X = [i_{s\alpha}\ i_{s\beta}\ \varphi_{r\alpha}\ \varphi_{r\beta}]^T$; $U = [u_{s\alpha}\ u_{s\beta}]^T$; $Y = [i_{s\alpha}\ i_{s\beta}]^T$ and

$$E = \begin{bmatrix} a_1 & a_2 & a_3 & a_4 \\ -a_2 & a_1 & -a_4 & a_3 \\ a_5 & 0 & a_6 & a_7 \\ 0 & a_5 & -a_7 & a_6 \end{bmatrix}; W = \begin{bmatrix} b_1 & 0 \\ 0 & b_1 \\ 0 & 0 \\ 0 & 0 \end{bmatrix}; M = \begin{bmatrix} 1 & 0 & 0 & 0 \\ 0 & 1 & 0 & 0 \end{bmatrix}$$

$$\begin{cases} a_1 = -\left(\frac{1}{\sigma T_s} + \frac{1-\sigma}{\sigma T_r}\right) \; ; \quad a_2 = 0 \quad ; \quad a_3 = \frac{1-\sigma}{\sigma T_r M} \\ a_4 = \frac{1-\sigma}{\sigma M}\omega \; ; \; a_5 = \frac{M}{T_r} \; ; a_6 = -\frac{1}{T_r} \quad ; \quad a_7 = -\omega \quad ; \quad b_1 = \frac{1}{\sigma L_s} \end{cases}$$

$$T_s = \frac{L_s}{R_s} \quad , T_r = \frac{L_r}{R_r} \quad , \sigma = 1 - \frac{M^2}{L_s L_r}$$

2.5. Modeling of the centrifuge pump

The square of the IM rotor speed defines the centrifugal pump load torque [53] which is expressed by $C_r = K_r \Omega^2$. Using similarity laws, the performances (Q_2, H_{mt2}, P_2) for any given speed N_2 can be established from nominal values (Q_1, H_{mt1}, P_1) at nominal speed N_1 as $Q_2 = \frac{N_2}{N_1} Q_1$, $H_{mt2} = \left(\frac{N_2}{N_1}\right)^2 H_{mt1}$ and $P_2 = P_1 \left(\frac{N_2}{N_1}\right)^3$.

The 1.5 kW IM is coupled to the chosen centrifugal pump, which has a nominal rotation speed of 1450 rpm, a flow rate of 15 m^3/h, and a manometric head of 20 m.

3. Control strategy of the PVPS

3.1. DC-DC boost converter controller

3.1.1. MPPT controller strategy

By adjusting its duty cycle α, the DC/DC boost serves to extract MPP from the PVG. In this paper, a combination of the incremental conductance algorithm (InC) and a super-twisting sliding mode controller is used, [54]. This strategy aims at forcing the PVPS to attain the MPP with excellent tracking performance and stability despite climate variations.

The control law in SMC requires the calculation of two parts. The state trajectory's attractivity to the sliding surface is covered in the first term, and the point's dynamic response is covered in the second. The control law is expressed as:

$$u = u_{eq} + u_{nl} \tag{12}$$

where u_{eq} is the equivalent control law tuned from cancelling the first time derivate of the sliding surface $(\dot{s}(x) = 0)$ and u_{nl} is a nonlinear term guarantee that the variable is attractive toward the commutation surface.

The super-twisting control law is developed to eliminate the chattering phenomenon [55-56]. The proposed MPPT strategy's block diagram has two nested loops. As seen in Fig. 6, an inner loop controls the inductor current while an outside loop sets the PVG voltage at its optimal level.

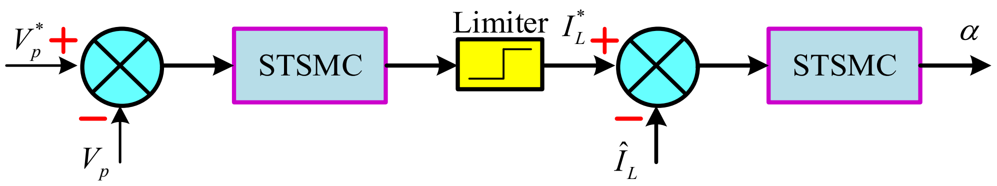

Fig. 6 Control of the DC-DC boost converter.

Following the state space model of a DC-DC boost converter, the sliding surface for the outer loop is defined as:

$$s_1 = \left(V_{pv}^* - V_{pv}\right) + \int \left(V_{pv}^* - V_{pv}\right) \tag{13}$$

where V_p^* represents the MPP reference voltage.

According to Eq. (**13**), the control law is chosen as follows:

$$I_L^* = I_{L\_eq} + I_{L\_n} \tag{14}$$

where:

$$\begin{cases} I_{L_n} = -a_1 |s_1|^{0.5}\, sign(s_1) + I_{L\_n_1} \\ \dot{I}_{L n_1} = -\beta_1\, sign(s_1) \end{cases} \tag{15}$$

and $a_1$and β_1 are positive constants.

The control term equivalent is derived from the invariance condition $\dot{s}_1 = 0$. Hence,

$$I_{L\_eq} = I_p - C_p\left(\dot{V}_{pv}^* + V_{pv}^* - V_{pv}\right) \tag{16}$$

To ensure the stability and robustness of the outer loop the condition $s_1 \dot{s}_1 < 0$ must be satisfied.

Hence, by substituting Eq. (**15**) and Eq. (**16**) into Eq. (**13**), from Eq. (**14**) we have:

$$\dot{s}_1 = \dot{V}_{pv}^* - \frac{1}{C_p}\left(I_{pv} - I_L\right) + \left(V_{pv}^* - V_{pv}\right) \tag{17}$$

After some algebra, we have:

$$s_1 \dot{s}_1 = -\frac{1}{C_p}\, s_1 \left(a_1 |s_1|^{0.5}\, sign(s_1) + \beta_1 \int sign(s_1)\right) < 0 \tag{18}$$

According to the result of Eq. (**18**), we can conclude that stability is ensured since s_1 and $\dot{s}_1$ are always of opposite signs.

For the inner loop, the sliding surface and the control law are defined as:

$$s_2 = \left(I_L - I_L^*\right) + \int \left(I_L - I_L^*\right) \tag{19}$$

$$\alpha = \alpha_{eq} + \alpha_n \tag{20}$$

where:

$$\begin{cases} \alpha_n = -a_2 |s_2|^{0.5}\, sign(s_2) + \alpha_{n_1} \\ \dot{\alpha}_{n_1} = -\beta_2\, sign(s_2) \end{cases} \tag{21}$$

where a_2 and β_2 are positive constants and the equivalent term is given by:

$$\alpha_{eq} = 1 - \frac{V_{pv} - L\left(\dot{I}_L^* - \left(I_L - I_L^*\right)\right)}{V_{dc}} \tag{22}$$

Similarly, the condition $s_2\dot{s}_2 < 0$ needs to be verified to confirm the inner loop's stability and robustness. The first derivative of s_2 gives:

$$\begin{aligned}\dot{s}_2 &= \left(\dot{I}_L - \dot{I}_L^*\right) + (I_L - I_L^*)\\ &= \frac{1}{L}(V_{pv} - (1-\alpha)V_{dc}) - \dot{I}_L^* + (I_L - I_L^*)\end{aligned} \tag{23}$$

Eq. (21) and Eq.(22) are substituted in Eq. (20) and using Eq.(23) it follows:

$$\begin{aligned}\dot{s}_2 = \frac{1}{L}\left(V_{pv} - (1 - (1 - \frac{V_{pv} - L\,(\dot{I}_L^* - (I_L - I_L^*))}{V_{dc}} - a_2|s_2|^{0.5} sign(s_2) - \beta_2 \int sign(s_2)))\,V_{dc}\right)\\ - \dot{I}_L^* + (I_L - I_L^*)\end{aligned} \tag{24}$$

After some algebra, we have:

$$s_2\dot{s}_2 = -\frac{V_{dc}}{L} \times s_2\left(a_2|s_2|^{0.5} sign(s_2) + \beta_2 \int sign(s_2)\right) < 0 \tag{25}$$

According to Eq. (25), we can conclude that the stability is ensured since s_2 and $\dot{s}_2$ are always of opposite sign.

3.1.2. Neural network observer for the inductor current

To improve the competitiveness of the system, the inductor current sensor has been removed and replaced with an NNO [57-59]. The NNO structure is illustrated in Figure 7. It consists of three layers: the input layer, which represents the PV array voltage and PV array current using two nodes, a hidden layer (HL) that models the nonlinear relationship between the system's inputs and outputs, and the output layer, where the inductor current I_L is the output variable. The characteristics of the NNO are detailed in Table 2.

The primary role of the NNO is to estimate the inductor current, which exhibits high-frequency characteristics, and to compensate for both internal and external perturbations, including model uncertainties, and external disturbances, in real time. Given the use of a single hidden layer, the NNO leverages its nonlinear approximation capabilities to model the fast dynamics of the inductor current and enhance state estimation accuracy. Mathematically, the estimated inductor current can be expressed as:

$$\hat{I}_L = \sum_{j=1}^{N} \omega_j^{(2)} . \sigma\left(\sum_{i=1}^{2} \omega_{ji}^{(1)} x_i + b_j^{(1)}\right) + b^{(2)} \tag{26}$$

where $\omega_{ji}^{(1)}$ and $b_j^{(1)}$ are the weights and biases of the hidden layer, σ is the hidden layer sigmoid activation function and x_i represents the inputs $\left(x_1 = V_{pv}, x_2 = I_{pv}\right)$, while $\omega_j^{(2)}$ and $b^{(2)}$ are the weights and biases of the output layer.

By addressing both internal perturbations—such as parametric variations and unmodeled dynamics—and external perturbations—such as load variations and weather conditions variation—the NNO significantly enhances system robustness. This contributes to improved control performance by mitigating modelling inaccuracies and enabling precise regulation. Additionally, the NNO reduces reliance on direct high-frequency current measurements, which can be challenging due to sensor limitations and noise. The use of the Levenberg-Marquardt algorithm for training the NN parameters ensures efficient convergence and optimizes the accuracy of inductor current estimation, making the system more resilient against disturbances and varying operating conditions.

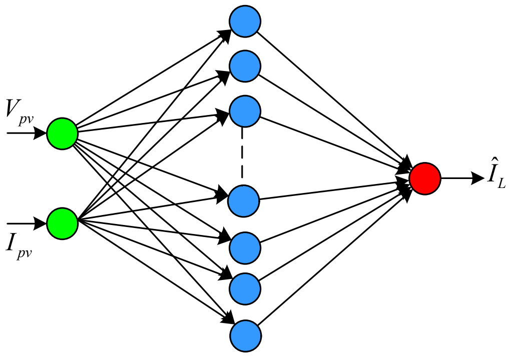

Fig. 7 Artificial neural network observer.

Table 2 Main features of the employed NNO.

Features	Value
Number of HL	1
Number of neurons in HL	20
HL activation function	sigmoid
Output layer activation function	linear
Cost function	MSE
Learning algorithm	Levenberg-Marquardt

3.2. Control of the IM

The objective to be achieved by the application of SMC combined with an oriented rotor field control (FOC) is to control the IM like an independent excitation DC machine. In this case, there is a natural decoupling between the parameter, which controls flux, and one that controls the torque, [42-43].

In FOC, the IM speed rotor is controlled by the quadrature component current i_{sq} whereas the flux is adjusted by the stator current's direct component i_{sd}[42-43]. The combination of SMC with FOC enhances the robustness of the IM speed control despite internal and/or external parameter uncertainties.

Two methods are used in this paper to estimate the IM rotor speed: LO and SMO. The advantages of the proposed control approach are demonstrated by comparing simulation results with FOC using PI controllers without a speed sensor in the presence of external perturbations (weather variations).

Table 3 lists the IM parameters that were used in the simulation.

Table 3 IM specifications and parameters

Parameters	Variable	Values
Stator and rotor resistances	R_s, R_r	4.58 Ω, 3.805 Ω
Stator and rotor inductances	L_s, L_r	0.274 H
Mutual inductance stator-rotor	M_{sr}	0.258 H
Pole pairs	p	2
Rated power	P_n	1.5 kW
Rotor inertia	j	0.0049 kg .m2
Rated speed	N_n	1450 rpm
Rated voltage	V_n	220 V

When the rotor flux is oriented with the d-axis, the model of the IM in the (d-q) reference frame is as follows:

$$\begin{cases} \frac{di_{sd}}{dt} = -\left(\frac{1}{\sigma T_s} + \frac{1-\sigma}{\sigma T_r}\right) i_{sd} + \omega_s i_{sq} + \frac{1-\sigma}{\sigma T_r M} \varphi_r + \frac{1}{\sigma L_s} v_{sd} \\ \frac{di_{sq}}{dt} = -\omega_s i_{sd} - \left(\frac{1}{\sigma T_s} + \frac{1-\sigma}{\sigma T_r}\right) i_{sq} - \frac{1-\sigma}{\sigma M} \omega \varphi_r + \frac{1}{\sigma L_s} v_{sq} \\ \frac{d\varphi_r}{dt} = \frac{M}{T_r} i_{sd} - \frac{1}{T_r} \varphi_r \\ 0 = \frac{M}{T_r} i_{sq} - \omega_g \varphi_r \end{cases} \tag{27}$$

where: $T_s = \frac{L_s}{R_s}$, $T_r = \frac{L_r}{R_r}$, $\sigma = 1 - \frac{M^2}{L_s L_r}$, $\omega_g = (\omega_s - \omega)$

To ensure that the pulsation ω_s is the same as the frame (d, q) pulsation:

$$\theta s = \int_0^t \omega_s dt \text{ where: } \omega_s = \omega + \omega_g \tag{28}$$

Eq. (27) provides the relationship between the estimated rotor flux and the stator current:

$$i_{sd} .\hat{\varphi} r = \frac{M}{1 + s \times T_r} i_{sd} \tag{29}$$

The slip pulsation ω_g and the electromagnetic torque are expressed by:

$$\omega_g = \frac{M}{T_r}\frac{i_{sq}}{\hat{\varphi}_r} \text{ and } \hat{C}_{em} = \frac{3}{2}p\frac{M}{L_r}\hat{\varphi}_r i_{sq} \tag{30}$$

The cascade structure of SMC applied to IM begins with determining the relative degree of each variable to be controlled. These variables are i_{sd}, φ_r, ω_r and i_{sq}. In the outer loops, the rotor flux and the IM rotor speed are controlled. The latter generates the references current i_{sd} and i_{sq} for the inner control loop. The control of (i_{sd}) and (i_{sq}) generates the reference voltages to be applied to the IM.

The IM reference speed corresponding to the output PV array power is given by the following equation, [3, 55]:

$$\omega_r^* = \sqrt[3]{\frac{\eta}{k_r} P_{pv}} \tag{31}$$

where η is the PVPS total efficiency.

In the proposed SMC-FOC scheme, we have defined four sliding surfaces:

$$\begin{aligned} S_{\omega r} &= \omega_r^* - \omega_r \\ S_\varphi &= \varphi_r^* - \varphi_r \\ S_{isd} &= i_{sd} - i_{sd}^* \\ S_{i_{sq}} &= i_{sq}^* - i_{sq} \end{aligned} \tag{32}$$

A saturation function Sat(x) is used in place of the sign function sign(x) to reduce the undesirable chattering noise it produces. Sat(x) is written as follows:

$$Sat(x) = \begin{cases} 1, x > \varepsilon \\ \frac{x}{\varepsilon}, |x| < \varepsilon \\ -1, x < \varepsilon \end{cases} \tag{33}$$

3.2.1. Rotor speed regulation

The rotor speed is controlled via i_{sq}:

$$i_{sq}^* = i_{sq\_eq} + i_{sq\_nl} \tag{34}$$

The equivalent term, i_{sq_eq} , is obtained by solving $\dot{S}_{\omega r} = 0$.

$$i_{sq\_eq} = \frac{2L_r j}{3pM\varphi_r}(C_r + f\omega_r) \tag{35}$$

The non-linear term in the control law is:

$$i_{sq\_nl} = k_\omega \times sat\left(\frac{S_{\omega r}}{\beta_\omega}\right) \tag{36}$$

where β_ω is a positive constant used to enhance the time response of the system. Finally, the control law can be designed as:

$$i_{sq}^* = \frac{2L_r j}{3pM\varphi_r}(C_r + f\omega_r) + k_\omega \times sat\left(\frac{S_{\omega r}}{\beta_\omega}\right) \tag{37}$$

3.2.2. Rotor flux regulation

The stator current's component i_{sd} controls the rotor flux. To regulate the rotor flux, the sliding surface is selected as:

$$S_\varphi = \varphi_r^* - \varphi_r \tag{38}$$

The control law is defined as:

$$i_{sd}^* = i_{sd\_eq} + i_{sd\_nl} \tag{39}$$

The equivalent term, i_{sd_eq} , is obtained by solving $\dot{S}_\varphi = 0$.

$$i_{sd\_eq} = \frac{\varphi_r}{M} \tag{40}$$

The nonlinear term is:

$$i_{sd\_nl} = k_\varphi \times sat\left(\frac{S_\varphi}{\beta_\varphi}\right) \tag{41}$$

where β_ω is a positive constant.

As a result, the reference current is of the form:

$$i_{sd}^* = \frac{\varphi_r}{M} + k_\varphi \times sat\left(\frac{S_\varphi}{\beta_\varphi}\right) \tag{42}$$

3.2.3. *Direct current regulation*

The quadrature component of the stator voltage V_{sd} controls the direct current i_{sd}. The selected sliding surface is:

$$S_{isd} = i_{sd} - i_{sd}^* \tag{43}$$

The control law is designed as:

$$V_{sd}^* = V_{sd\_eq} + V_{sd\_nl} \tag{44}$$

The equivalent term is obtained by $\dot{S}_{\mathrm{isd}} = 0$, this leads to:

$$V_{sd\_eq} = \sigma L_s \frac{di_{sd}^*}{dt} + \left(Rr + \left(\frac{M^2}{T_r L_r}\right)\right) i_{sd} - \sigma L_s \omega_s i_{s_d} - \left(\frac{M}{T_r L_r}\right) \varphi_r \tag{45}$$

where:

$$\frac{di_{sd}}{dt} = \frac{1}{\sigma L_s}\left(V_{sd} - \left(Rr + \left(\frac{M^2}{T_r L_r}\right)\right) i_{sd} + \sigma L_s \omega_s i_{s_d} + \left(\frac{M}{T_r L_r}\right) \varphi_r\right)$$

The nonlinear component of the voltage is:

$$V_{sd\_nl} = -k_{isd} \times sat\left(\frac{S_{isd}}{\beta_{isd}}\right) \tag{46}$$

Finally, the direct component of reference voltage is given by:

$$V_{sd}^* = \sigma L_s \frac{di_{sd}^*}{dt} + \left(Rr + \left(\frac{M^2}{T_r L_r}\right)\right) i_{sd} - \sigma L_s \omega_s i_{s_d} - \left(\frac{M}{T_r L_r}\right) \varphi_r - k_{isd} \times sat\left(\frac{S_{isd}}{\beta_{isd}}\right) \tag{47}$$

3.2.4. *Quadrature current regulation*

The reference quadrature voltage component is given by:

$$V_{sq}^* = \left(\sigma L_s \frac{di_{sq}^*}{dt} + \left(Rr + \left(\frac{M^2}{T_r L_r}\right)\right) i_{sq} + \sigma L_s \omega_s i_{sd} - \frac{M_{sr}}{L_r} \varphi_r\right) + k_{isq} \times sat\left(\frac{S_{isq}}{\beta_{isq}}\right) \tag{48}$$

3.2.5. *Design of sliding mode IM rotor speed observer*

To ensure the correct operation of SMC with FOC, it is necessary to have excellent information on the state variables of the IM to be controlled; this requires use of electrical sensors (current, voltage) and mechanical speed sensors. However, the system's complexity and cost increase when sensors are used. Indeed, the substitution of these sensors by observers, based on the measurement of the state variables of IM, makes the structure more competitive [60-63].

The IM model, given here above, can be expressed differently in matrix form as:

$$\begin{cases} \begin{bmatrix} \dfrac{di_{s\alpha}}{dt} \\ \dfrac{di_{s\beta}}{dt} \end{bmatrix} = k_1\left(\begin{bmatrix} \lambda & \omega_r \\ \omega_r & \lambda \end{bmatrix}\begin{bmatrix} \varphi_{r\alpha} \\ \varphi_{r\beta} \end{bmatrix} - \lambda M \begin{bmatrix} i_{s\alpha} \\ i_{s\beta} \end{bmatrix}\right) - k_2 \begin{bmatrix} i_{s\alpha} \\ i_{s\beta} \end{bmatrix} + k_3 \begin{bmatrix} u_{s\alpha} \\ u_{s\beta} \end{bmatrix} \\ \begin{bmatrix} \dfrac{d\varphi_{r\alpha}}{dt} \\ \dfrac{d\varphi_{r\beta}}{dt} \end{bmatrix} = -\left(\begin{bmatrix} \lambda & \omega_r \\ \omega_r & \lambda \end{bmatrix}\begin{bmatrix} \varphi_{r\alpha} \\ \varphi_{r\beta} \end{bmatrix} - \lambda M \begin{bmatrix} i_{s\alpha} \\ i_{s\beta} \end{bmatrix}\right) \end{cases} \tag{49}$$

where:

$$k_1 = \frac{M}{L_r L_s \sigma} = \frac{k_3 M}{L_r}; k_2 = \frac{R_s}{\sigma L_s}; k_3 = \frac{1}{\sigma L_s} \text{ and } \lambda = \frac{1}{T_r}$$

After some algebra, the estimated speed $\hat{\omega}_r$ can be calculated as:

$$\hat{\omega}_r = \frac{E_\alpha \hat{\varphi}_{r\beta} - E_\beta \hat{\varphi}_{r\alpha} - \lambda M\left(\hat{\varphi}_{r\alpha}\hat{\imath}_{s\beta} - \hat{\varphi}_{r\beta}\hat{\imath}_{s\alpha}\right)}{\hat{\varphi}^2{}_{r\alpha} + \hat{\varphi}^2{}_{r\beta}} \tag{50}$$

It is worth to mention that in the last five subsections, stability analysis has been verified through the derivative of the Lyapunov functions which are found negative definite. This means, based on Lyapunov stability theory, that the observer is asymptotically stable.

4. Simulation test validation

The two-stage PVPS simulation results are examined in this section. In the simulation, the nominal power of the IM and the load torque constant applied by the pump on the IM shaft were fixed to 1.5 kW and K_r=0.0004072, respectively.

To track the maximum power from the PVG, two variables must be sensed GPV voltage and GPV current. In this work, the InC-STSMC is adopted as detailed in section 2.

To reduce the system cost, the inductor current of the DC-DC boost converter is estimated using two methods: NNO and sliding mode observer (SMO) [**64**] as shown in Fig.1.

For the conception of the ANN observer, learning is performed offline. The training data are collected from the simulation using Matlab-Simulink. The collected data consists of 600000 samples of inductor current I_L, PV array voltage V_p and PV array current values I_p. This data set is divided into three parts, the first data set, which represents 70 %, is used for the learning process of the ANN, the second data set, representing 15%, is used for validation and the last one, representing 15 % of the collected data, is used to test the performance of the ANN.

Results of the training, validation and test phases are shown in Fig.8 and Fig.9. The Mean Squared Error (MSE) method is used for error calculation during the learning process.

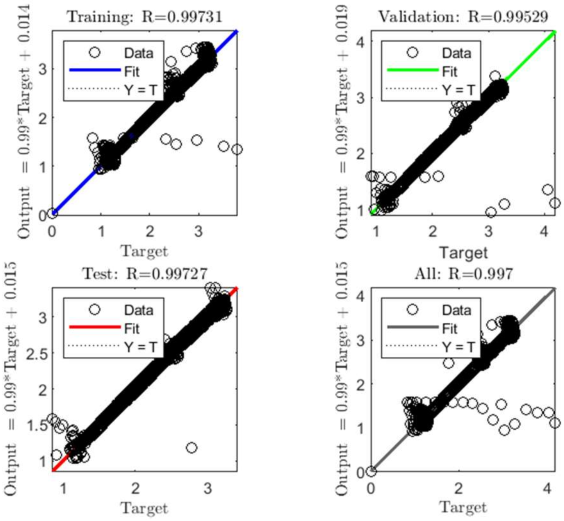

Fig. 8 Regression performance.

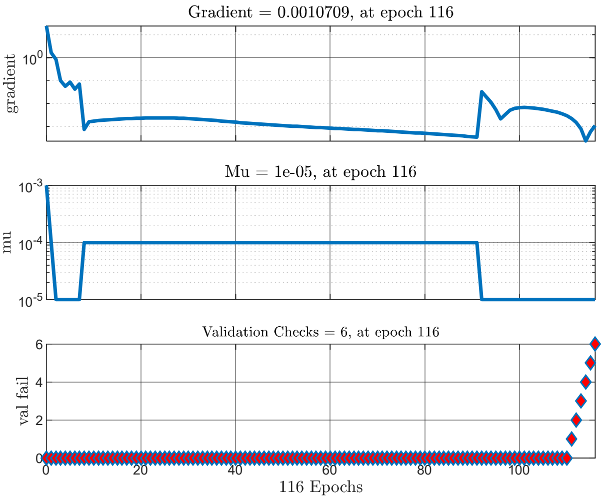

Fig. 9 The neural network training.

From the Fig.10.d, the NNO method is retained since it presents less oscillation rate (0.6 %) than SMO method (3.31 %). The response time is similar for the two observers (~16 ms).

Table 4 Comparative performance of speed observer variation.

Observer	Response time (s)	Error estimation (%)	Oscillations (rad/s)	Overshoot (%)
SMO	0.0162	0.67	1	0.5
LO	0.0165	3.3	5	2

To study the robustness of the PVPS when using InC-STSMC for MPPT controller and the SMC-FOC for IM control, variable irradiation is applied to the PVPS while the temperature is kept constant (T=25 °C) as seen in Fig.10.a. Simulation results in Fig.10.b and Fig.10.c clearly show that the system is stable for any sudden variation in irradiation, the MPP is well tracked in short settlement time. The GPV power varies from 1.88 kW to 1.156 kW when the solar irradiation changes from 1000 W/m2 to 600 W/m2, respectively.

The evolution of speed rotor and flow rate when using SMC and PI strategies with rotor speed sensors are shown in Figs. 11. a and 11.d. Fig.11.a shows large steady-state oscillations using PI regulators compared to the structure based on SMC. During the transient state as shown in Fig.11.b, the stator current shows a higher peak value when using PI control method compared to using SMC. Furthermore, a zoomed view at Figs. 11. c and 12. b reveals that the rotor flux converges to 0.85 Wb, which is their reference value.

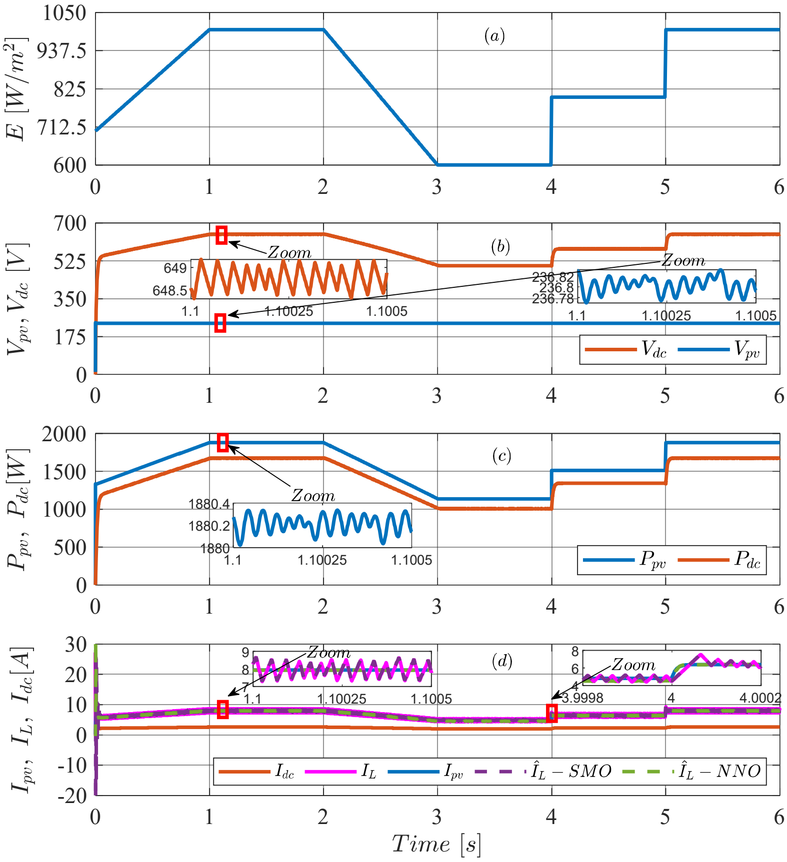

Fig. 10 Performance of PV array.

The chattering phenomena in the SMC resulted in small oscillation, as shown in Fig.12. The simulation results obtained clearly demonstrate the effectiveness of the use of the Sat function. Indeed, the rotor speed oscillations are attenuated when compared to those of conventional PI controllers, as shown in Figs. 11.a and 12. d. The static error caused is of a barely detectable amplitude, especially since it is instantly rejected. Nevertheless, we notice residual oscillations on the direct and quadratic stator current when it reaches the steady state, which correspond to an oscillation around the sliding surface, but which are attenuated very quickly because the control passes from the discontinuous control to the continuous control and the system enters a sliding mode around $\mathrm{S(x)} = 0$ as seen in Fig.12.a and Fig.12.c.

Given the obtained results with the different types of controllers and surfaces, we conclude that the speed response obtained with the SMC is faster than that obtained with the classical PI controller [**65**]. The speed error is compensated instantaneously, while that of the classic vector control is compensated only after a certain time. The gains of the discontinuous control $\mathrm{k}_{\omega}, \mathrm{k}_{\varphi}, \mathrm{k}_{\mathrm{isd}}$ and $\mathrm{k}_{\mathrm{isq}}$ are very difficult to manipulate because too small values lead to slow system dynamics and too large values amplify the chattering phenomenon. This phenomenon was attenuated by the « Sat » function.

5. The Results of Experimental Studies

In this section, the nonlinear InC-STSMC controller with NNO designed in paragraph **3.1** was verified and validated using MIL and PIL tests. During the PIL simulation, the host and the microprocessor process at each iteration the data in semi-real time [**66**]. Using these prototyping steps accelerates design, tests as many scenarios as possible, and improves system control quality, while reducing the need for real prototypes and physical testing.

The performance of a portion of the simulated system is tested on a host by running the InC-STSMC with NNO on target via C code generation. STM32F769I is one of the many available options for PIL simulation. The STM 32 ARM Cortex M7 32-bit microcontroller was chosen because of its accessibility, high speed, quick processing, and simplified handling features. Host-target communication, during PIL simulation, is done through a low-speed ST-link or by a high-speed USB USART converter. For the prepared simulation, we used the ST-link communication.

STM32F core with cortex M7 is much easier compared to Dspace and FPGA cores [67]. In addition, it is faster (216 MHz) with respect to Dspace, which has a clock speed limited to 40 MHz [67]. Fig.13 shows the optimized C code generation for a 32-bit ARM cortex M7 microcontroller of the STSMC without an inductor current sensor. It is co-simulated via PIL test in the low-cost STM32F769I discovery board.

The decision not to integrate the induction motor (IM) control directly into the processor and to partition the control functions between the photovoltaic (PV) and pumping systems is based on several key factors. First, hardware constraints play a crucial role. As demonstrated in the study [68-69], asynchronous architectures and specialized processors (FPGA, DSP) are better suited for complex nonlinear computations. Thus, the STM32F769I is dedicated to InC-STSMC with NNO, while the more computationally demanding FO-SMC and SMO for IM control are externalized to prevent resource overload. Additionally, this task partitioning ensures dynamic and efficient resource allocation [70-71]. Running NNO and STSMC on the microcontroller while offloading FO-SMC to Simulink optimizes both latency and power consumption [72]. Moreover, separating the PV and pumping control enhances system modularity and scalability. Progressive validation through PIL testing ensures robustness and minimizes modelling errors [73]. Furthermore, transitioning to FPGA/DSP architectures would enable real-time adaptability to motor control requirements [71, 74]. Finally, the need for rapid adaptation to weather conditions variations justifies this separation. InC-STSMC with NNO must respond instantly to irradiance and temperature change, whereas FO-SMC and SMO for motor control handle different load variations to enhance stability and disturbance management [70, 74-75]. Thus, this approach ensures an optimal balance between performance, modularity, and scalability, while effectively managing hardware and computational constraints.

Variable irradiation, as shown in Fig.10.a, and a constant temperature (T=25 °C) are the weather conditions applied for MIL and PIL simulation test of the PVPS. In addition, the values of coefficients in the method of STSMC with NNO used in MIL and PIL simulations are the same.

Fig.14 shows the effectiveness of the InC-STSMC with NNO in tracking the MPP, demonstrating that the designed sensor-less controller does not oscillate around the MPP.

Fig.14. c depicts an instantaneous estimation error of the inductor current, which is quickly reduced to zero during the estimation process at 0.3 s, confirming the performance of the NNO. In addition, the PV output voltage is stabilized at its reference value, as illustrated in Fig. 14.a. As seen in Fig.14.b, the GPV power successfully tracked its theoretical maximum value for 1.88 kW at the standard’s test condition (1 kW/m², 25°C). The PIL simulation results clearly show that the inductor current was predicted with an average error of less than 1% in terms of its simulation value. Based on these results, the use of the NNO to estimate the inductor current value was computed with effectiveness. The error between MIL and PIL tests results is almost zero, which signifies that InC-STSMC with NNO during PIL testing process and in the simulation environment under MATLAB/Simulink are the same.

A zoomed view, in Fig.15, shows that the PIL test of the proposed InC-STSMC does not affect the application of indirect field-oriented sliding mode control also provides the operating of IM wherein the flux linkage is decoupled to rotor speed. In fact, during the operation, speed rotor and flow rate are maintained at their reference value, this even in sudden weather condition variation, and hence only variation in the transient period was noted, as shown in Fig.15.a and Fig.15.d, respectively. In addition, rotor flux meets to their reference value (0.85 Wb) as presented in Fig.15.c. Figs. 14 and 15 show that the PIL and MIL simulation results are almost similar.

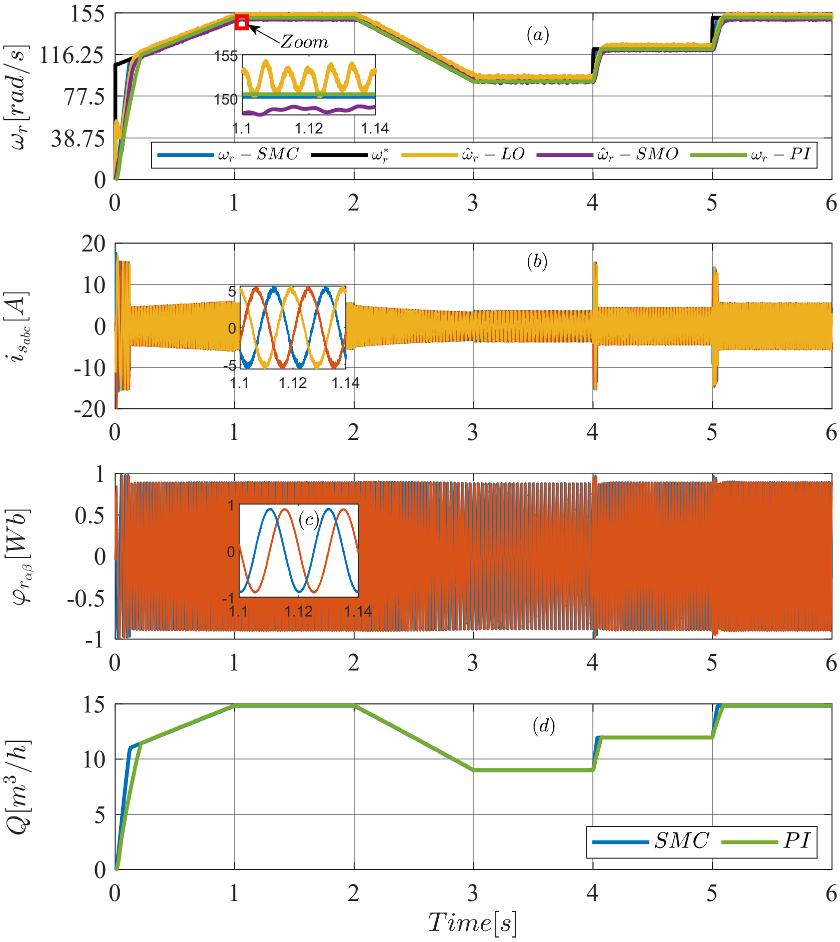

Fig. 11 IM performance with SMC and PI controller-based speed estimation during varying weather conditions.

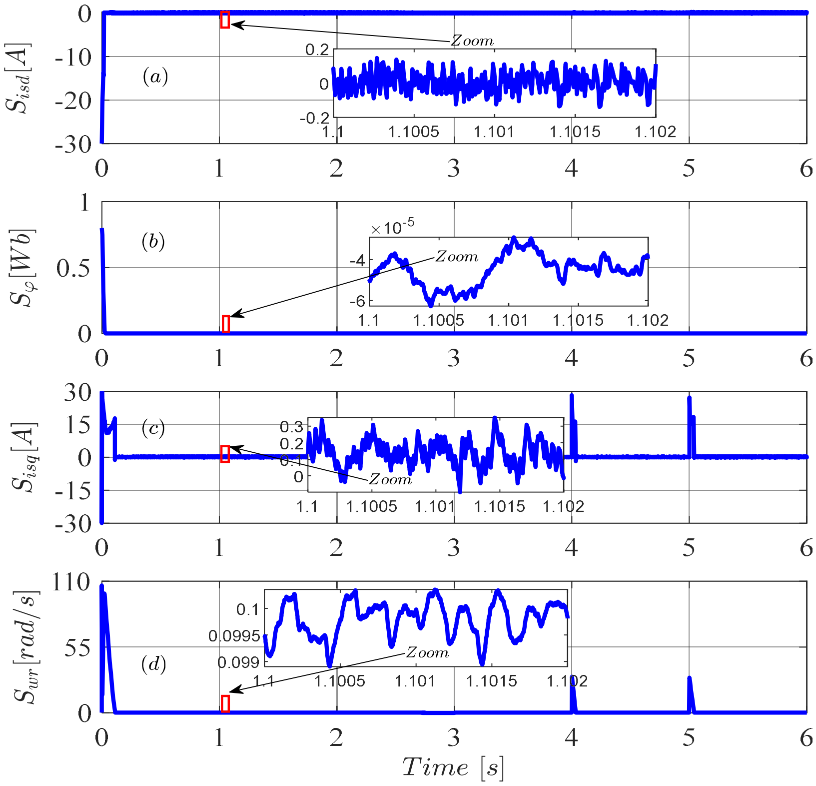

Fig. 12 Sliding surface.

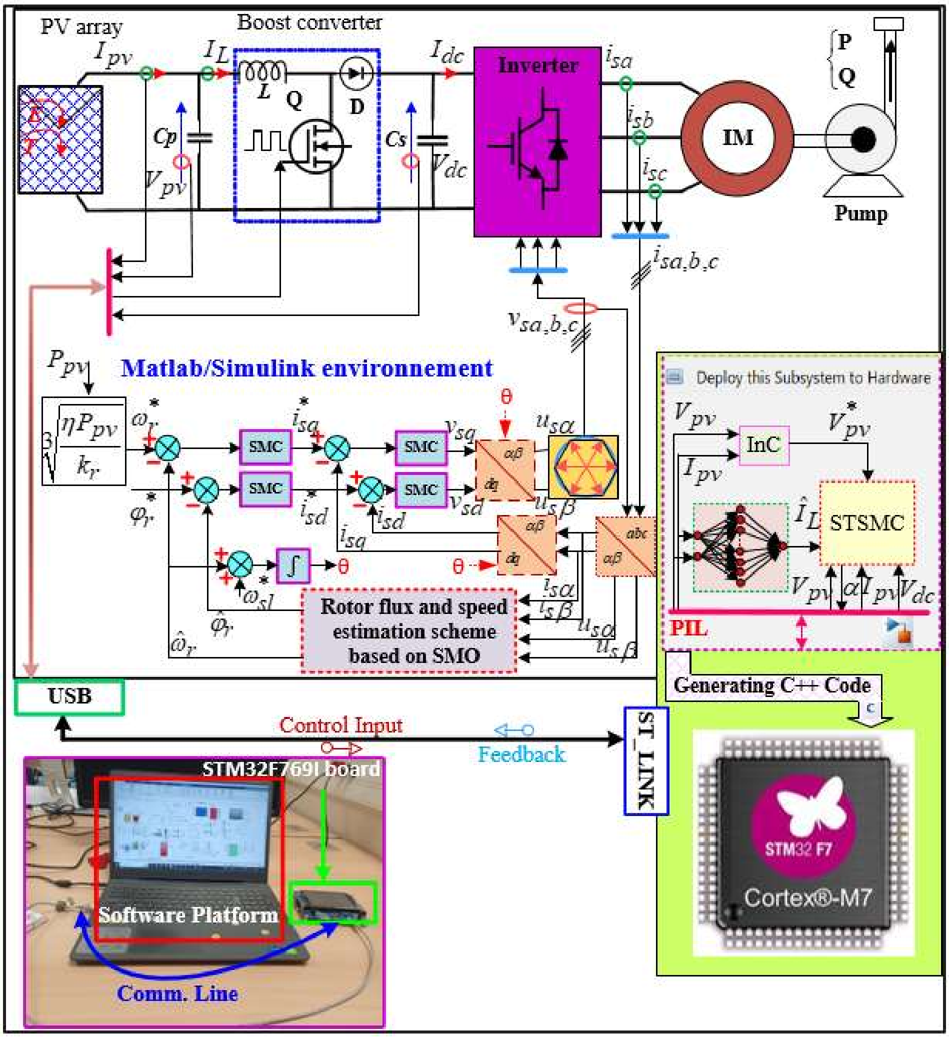

Fig. 13 The overall PIL test setup

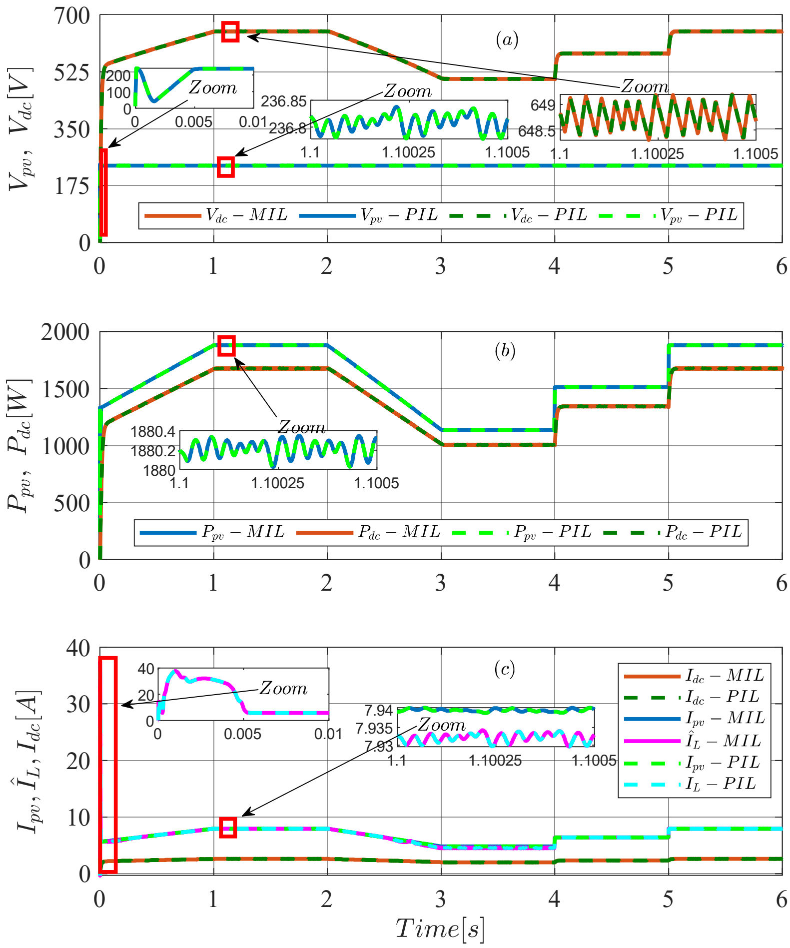

Fig. 14 The output of PV array obtained from MIL and PIL simulation.

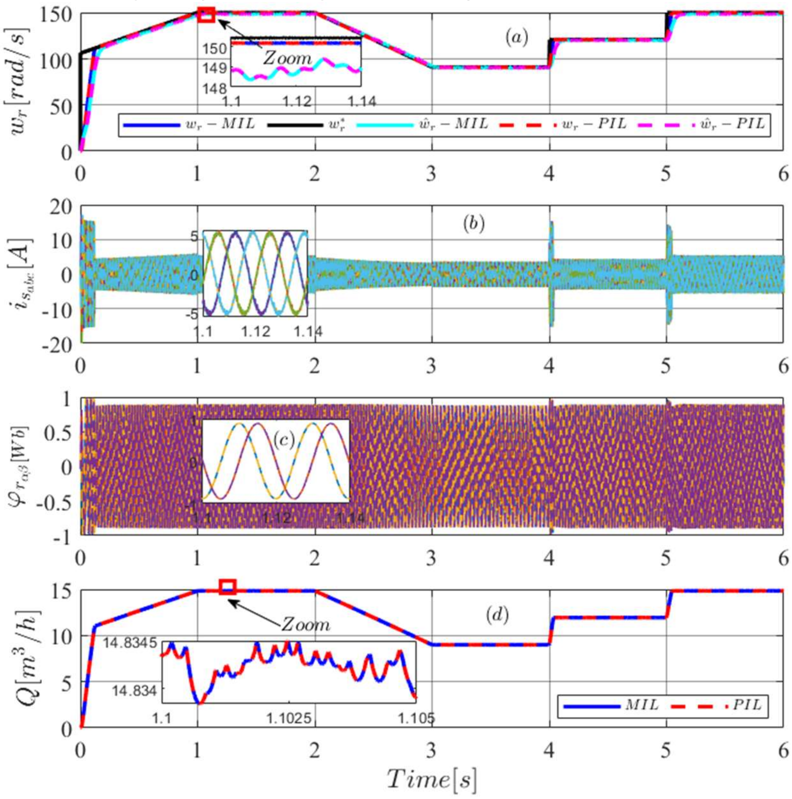

Fig. 15 Output waveform of the IM obtained when using NNO for MIL and PIL test.

6. Conclusion

This paper presents a comprehensive study of a three-phase photovoltaic pumping system (PVPS) designed for enhanced efficiency and robustness. The system incorporates several advanced features, including a 1.5 kW three-phase induction motor, a three-phase voltage source inverter, and a DC-DC boost converter to maximize power extraction from a 1.88 kWp photovoltaic generator. The authors have focused on developing a low-cost, high-efficiency, and robust system suitable for remote agricultural areas where access to conventional power sources is limited.

The key highlights of this study include:

- Implementation of a hybrid incremental conductance super-twisting sliding mode controller (InC-STSMC) for maximum power extraction from the photovoltaic generator, enhancing the system's resilience against internal and external disturbances.
- Adoption of a flux-oriented sliding mode vector control (FO-SMC) for controlling the motor speed, improving stability and robustness.
- Use of a nonlinear neural network state observer (NNO) to monitor the inductor current and a sliding mode observer (SMO) to estimate the motor speed, reducing overall system cost by eliminating the need for physical sensors.
- Validation of the proposed control techniques through model-in-the-loop (MIL) simulations in the Matlab-Simulink environment, demonstrating significant improvements in dynamic performance compared to traditional proportional-integral (PI) approaches.
- Practical implementation and testing of the InC-STSMC with the NNO scheme using a processor-in-loop (PIL) test on an STM32F769I board.

The research presented in this paper offers a promising solution for efficient and reliable water pumping in remote agricultural areas, leveraging renewable energy sources. The proposed system's ability to operate stably under varying weather conditions and internal parameter uncertainties makes it particularly suitable for challenging environments. Future work in this area could focus on further optimizing the system's performance, exploring additional energy storage options, and conducting long-term field tests to validate the system's durability and effectiveness in real-world scenarios.

Nomenclature

PVPS	:	Photovoltaic pumping system
PVG	:	Photovoltaic generator
PV		Photovoltaic
VSI	:	Voltage source inverter
IM	:	Induction machine
NNO	:	Nonlinear neural network state observer
SMO	:	Sliding mode observer
SMC	:	Sliding mode controller
STSMC	:	Super-twisting sliding mode controller
FO-SMC	:	Flux-oriented sliding mode vector control
MIL	:	Model-in-the-loop
PI	:	Proportional-integral
PIL	:	Processor-in-loop
WPS	:	Water pumping systems
MPPT	:	Maximum power point tracking
MPP	:	Maximum power point
PO	:	Perturb & observe
FLC	:	Fuzzy logic
InC	:	Incremental conductance
DTC	:	Conventional direct torque control
InC-STSMC	:	Hybrid incremental conductance/super-twisting controller
LO	:	Luenberger observer
AC	:	Alternative current

DC	:	Direct current
$(\alpha - \beta)$	:	Clarke transformation
$(d - q)$	:	Park transformation
SVPWM	:	Space Vector Pulse Width Modulation
$S(x)$	:	Sliding surface
u_{eq}	:	Equivalent control law
u_{nl}	:	Nonlinear control law
HL	:	Hidden layer
N_p, N_s	:	Parallel branches of series PV modules
I_s	:	Cell's dark saturation current (A)
q	:	Charge of an electron ($q = 1.61 \times 10^{-19} C$)
k	:	Boltzmann's constant ($k = 1.38\ \times 10^{-23}\ J/K$),
T	:	Temperature of the PV module (°K)
A	:	Ideality factor
R_{sh}	:	Shunt resistance of the PV cell (Ω)
R_s	:	Series resistance of the PV cell (Ω)
K_H	:	Hydraulic constant
Q	:	Flow rate (m3/Hours);
H_{mt}	:	Manometric head (m);
t_h	:	Pumping operating time (hours),
η_{pm}	:	Motor-pump efficiency (%)
P_{pv}	:	PVG power (W)
V_{pv}	:	PV array voltage (V)
I_{pv}	:	PV array current (A)
f_s	:	Switching frequency (Hz)
$\Delta \mathrm{I_L}$	:	Current ripple through the boost inductor (A)
$\mathrm{I_L}$	:	Inductor current of boost converter (A)
α	:	Duty cycle of the boost converter
$\mathrm{V_{dc}}$	:	Input DC bus voltage of the VSI (V)
I_{dc}	:	Maximum current motor phase (A)
$V_{VSI}\ and\ I_{VSI}$	:	Voltage and current of an IGBT switch of the VSI (V/A)
V_α, V_β	:	Stator and rotor voltage in the $(\alpha - \beta)$ frame (V)
$\mathrm{L_s}$, $\mathrm{L_r}$ and M	:	Stator, rotor, and mutual inductance (H)
$\mathrm{I_{s\alpha}}$, $\mathrm{I_{s\beta}}$, $\mathrm{I_{r\alpha}}$, and $\mathrm{I_{r\beta}}$	:	Stator and rotor current in the $(\alpha - \beta)$ frame (A)
$\mathrm{R_s}$ and $\mathrm{R_r}$	:	Stator and rotor resistance (Ω)
K_r and Ω	:	Torque constant and the angular rotational speed of the pump
N	:	Rotation speed (rpm)
ω_s	:	Stator pulsation (rad/s)
ω_g	:	Slip pulsation (rad/s)
i_{sd}	:	d-axis current (A)
i_{sq}	:	Quadrature current (A)
ω_r	:	Rotor speed (rad/s)
φ_r	:	Rotor flux (Wb)
ω_r^*	:	IM reference speed (rad/s)
$\hat{\varphi}_{r\alpha}$and $\hat{\varphi}_{r\beta}$	:	α and β components of the rotor flux observed
$\hat{\imath}_{s\alpha}$ and $\hat{\imath}_{s\beta}$	:	observed α and β stator currents
$\tilde{\imath}_{s\alpha}$ and $\tilde{\imath}_{s\beta}$	:	α and β dynamic errors current
$\tilde{\varphi}_{r\alpha}$ and $\tilde{\varphi}_{r\beta}$	:	α and β dynamic errors rotor flux

- **Declaration of Competing Interest:** The authors declare that they have no conflict of interest or known competing financial interests or personal relationships that could have appeared to influence the work reported in this paper.
- **Authors' contributions:** Conceptualization, M.B., B.L., R.D.; Methodology, M.B., B.L., R.D., L.K., R.B.; Software, F.L., A.S.; Validation, M.B., B.L., R.D., L.K., R.R., R.B.; Formal Analysis, M.B.,

B.L., R.D., L.K., R.R., R.B.; Investigation, M.B., B.L., R.D., L.K., R.R., R.B.; Resources, M.B., B.L., R.D., L.K., R.R., R.B., F.L., A.S.; Data Curation, M.B., B.L., R.D., L.K., R.R., R.B.; Writing - Original Draft Preparation, M.B., B.L., R.D.; Writing - Review & Editing, M.B., B.L., R.D., L.K., R.B., F.L., A.S.; Visualization, F.L., A.S.; Supervision, M.B., B.L., R.D.; Project Administration, M.B., B.L. All authors read and approved the final manuscript.

- **Consent for publication:** not applicable.
- **Ethics approval and consent to participate**: not applicable.
- **Funding:** No funding received.
- **Availability of data and materials:** The datasets used in this study were generated using the personal computer and materials of the first author. Requests for access to the data should be directed to the corresponding author.
- **Dual publication:** The results/data/figures in this manuscript have not been published elsewhere, nor are they under consideration by another publisher.
- **Acknowledgements:** not applicable.

References

1. A. A. Yahyaoui, F. Tadeo, and G. M. Tina, "Energetic and economic sensitivity analysis for photovoltaic water pumping systems," *Solar Energy*, 144, no. 1 (2017): 376-391.
2. D. Gherbi, A. Hadj Arab, and H. Salhi, "Improvement and validation of PV motor-pump model for PV pumping system performance analysis," *Solar Energy*, 144, no. 1 (2017): 310-320.
3. B. Singh, U. Sharma, and S. Kumar, "Standalone photovoltaic water pumping system using induction motor drive with reduced sensors," *IEEE Transactions on Industry Applications*, 54, no. 4 (2018): 1-1.
4. H. Husaini, S. A. Mansor, and H. H. Lean, "Income inequality, natural resources dependence and renewable energy," *Resources Policy*, 89 (2024): 104480.
5. M. Musio, A. Serpi, C. Musio, and A. Damiano, "Optimal management strategy of energy storage systems for RES-based microgrids," *IECON 2015 - 41st Annual Conference of the IEEE Industrial Electronics Society*, (2015): 1-1.
6. M. A. Vitorino, M. B. R. Correa, C. B. Jacobina, and A. M. N. Lima, "An effective induction motor control for photovoltaic pumping," *IEEE Transactions on Industrial Electronics*, 58 (2011): 1162–1170.
7. F. Zaouche, D. Rekioua, J.-P. Gaubert, and Z. Mokrani, "Supervision and control strategy for photovoltaic generators with battery storage," *International Journal of Hydrogen Energy*, 42, no. 30 (2017): 19536–19555.
8. B. A. Bhayo, H. H. Al-Kayiem, and S. I. Gilani, "Assessment of standalone solar PV-battery system for electricity generation and utilization of excess power for water pumping," *Solar Energy*, 194 (2019): 766-776.
9. O. Okoye and O. Solyalı, "Optimal sizing of stand-alone photovoltaic systems in residential buildings," *Energy*, 126 (2017): 573–584.
10. B. K. Das, Y. M. Al-Abdeli, and G. Kothapalli, "Optimisation of stand-alone hybrid energy systems supplemented by combustion-based prime movers," *Applied Energy*, 196 (2017): 18–33.
11. T. Maatallah, N. Ghodhbane, and S. Ben Nasrallah, "Assessment viability for hybrid energy system (PV/wind/diesel) with storage in the northernmost city in Africa, Bizerte, Tunisia," *Renewable and Sustainable Energy Reviews*, 59 (2016): 1639–1652.
12. Mohammedi, D. Rekioua, T. Rekioua, and N. E. Mebarki, "Comparative assessment for the feasibility of storage bank in small scale power photovoltaic pumping system for building application," *Energy Conversion and Management*, 172 (2018): 579–587.

13. M. Errouha, A. Derouich, S. Motahhir, O. Zamzoum, N. El Ouanjli, and A. El Ghzizal, "Optimization and control of water pumping PV systems using fuzzy logic controller," *Energy Reports*, 5 (2019): 853-865.
14. G. Belgacem, "Performance of submersible PV water pumping systems in Tunisia," *Energy for Sustainable Development*, 16, no. 4 (2012): 415–420.
15. Selma, E. Bounadja, B. Belmadani, and B. Selma, "Improved performance and robustness of synchronous reluctance machine control using an advanced sliding mode and direct vector control," *Adv. Control. Appl. Eng. Ind. Syst.*, 6 (2024): e178.
16. O. Elbaksawi, "Design of photovoltaic system using buck-boost converter based on MPPT with PID controller," *Univers. J. Electr. Electron. Eng.*, 6 (2019): 314–322.
17. B. Kanouni, A. E. Badoud, S. Mekhilef, M. Bajaj, and I. Zaitsev, "Advanced efficient energy management strategy based on state machine control for multi-sources PV-PEMFC-batteries system," *Sci. Rep.*, 14 (2024): 7996.
18. J. Mehta and B. B. Naik, "Adaptive sliding mode controller with modified sliding function for DC-DC boost converter," *Power Electronics, Drives and Energy Systems (PEDES), 2014 IEEE International Conference on*, (2014): 1–5.
19. H. R. Koofigar, "Adaptive robust maximum power point tracking control for perturbed photovoltaic systems with output voltage estimation," *ISA transactions*, 60 (2016): 285–293.
20. S. K. Pandey, S. L. Patil, and S. B. Phadke, "Regulation of non-minimum phase DC-DC converters using integral sliding mode control combined with disturbance observer," *IEEE Trans. Circuits Syst. II*, (2017): 1–1.
21. H. R. Koofigar, "Adaptive robust maximum power point tracking control for perturbed photovoltaic systems with output voltage estimation," *ISA Transactions*, 60 (2016): 285-293.
22. S. V. Malge, M. G. Ghogare, S. L. Patil, A. S. Deshpande, and S. K. Pandey, "Chatter-free non-singular fast terminal sliding mode control of interleaved boost converter," *IEEE Transactions on Circuits and Systems II: Express Briefs*, 70, no. 1 (2022): 186-190.
23. L. Ardhenta and M. Rusli, "Sliding mode control of output voltage in DC-DC boost converter using PI sliding surface," *2021 International Conference on Electrical and Information Technology (IEIT)*, (2021): 228-232.
24. S. K. Pandey, S. L. Patil, U. M. Chaskar, and S. B. Phadke, "State and disturbance observer-based integral sliding mode controlled boost DC-DC converters," *IEEE Transactions on Circuits and Systems II: Express Briefs*, (2018): 1–1.
25. Kelkoul and A. Boumediene, "Stability analysis and study between classical sliding mode control (SMC) and super twisting algorithm (STA) for doubly fed induction generator (DFIG) under wind turbine," *Energy*, (2020): 118871.
26. R. Benadli, D. Frey, Y. Lembeye, M. Bjaoui, B. Khiari, and A. Sellami, "A direct backstepping super-twisting algorithm controller MPPT for a standalone photovoltaic storage system: Design and real-time implementation," *ASME. J. Sol. Energy Eng.*, 145, no. 6 (2023): 061002.
27. H. Kim and Y. I. Son, "Regulation of a DC/DC boost converter under parametric uncertainty and input voltage variation using nested reduced-order PI observers," *IEEE Transactions on Industrial Electronics*, (2016): 1–1.
28. Talbi, F. Krim, A. Laib, A. Sahli, and A. Krama, "PI-MPC switching control for DC-DC boost converter using an adaptive sliding mode observer," *2020 International Conference on Electrical Engineering (ICEE)*, (2020): 1-5.
29. H. Cho, S. J. Yoo, and S. Kwak, "State observer-based sensorless control using Lyapunov's method for boost converters," *IET Power Electronics*, 8, no. 1 (2015): 11-19.
30. M. Bjaoui, B. Khiari, R. Benadli, M. Memni, and A. Sellami, "Practical implementation of the backstepping sliding mode controller MPPT for a PV-storage application," *Energies*, 12, no. 18 (2019): 1-22.
31. S. Ahmed, H. M. Muhammad Adil, I. Ahmad, M. K. Azeem, Z. e Huma, and S. Abbas Khan, "Supertwisting sliding mode algorithm-based nonlinear MPPT control for a solar PV system with artificial neural networks-based reference generation," *Energies*, 13 (2020): 3695.

32. J. Fei and D. Jiang, "Fuzzy neural network sliding-mode controller for DC-DC buck converter," *IEEE Internet of Things Journal*, 11, no. 19 (2024): 31575-31586.
33. K. Singha and S. Kapat, "A unified framework for analysis and design of a digitally current-mode controlled buck converter," *IEEE Trans. Circuits Syst. I*, 63, no. 11 (2016): 2098–2107.
34. T. Hausberger, A. Kugi, A. Eder, and W. Kemmetmüller, "High-speed nonlinear model predictive control of an interleaved switching DC/DC-converter," *Control Engineering Practice*, 103 (2020): 104576.
35. K. Singha and S. Kapat, "A unified framework for analysis and design of a digitally current-mode controlled buck converter," *IEEE Trans. Circuits Syst. I*, 63, no. 11 (2016): 2098–2107.
36. H. P. Forghani-Zadeh and G. A. Rincon-Mora, "Current-sensing techniques for DC-DC converters," *2002 45th Midwest Symposium on Circuits and Systems*, 2 (2002): II.
37. Z. M. S. Elbarbary, O. K. Al-Harbi, S. F. Al-Gahtani, S. M. Irshad, A. Y. Abdelaziz, and M. A. Mossa, "Review of speed estimation algorithms for three-phase induction motor," *MethodsX*, 12 (2024): 102546.
38. Das, S. Madichetty, and B. Singh, "Luenberger observer-based current estimated boost converter for PV maximum power extraction—A current sensorless approach," *IEEE Journal of Photovoltaics*, (2018): 1–1.
39. Q. Tong, C. Chen, Q. Zhang, and X. Zou, "A sensorless predictive current controlled boost converter by using an EKF with load variation effect elimination function," *Sensors*, 15 (2015): 9986–10003.
40. H. Cho, S. J. Yoo, and S. Kwak, "State observer-based sensorless control using Lyapunov's method for boost converters," *IET Power Electronics*, 8, no. 1 (2015): 11-19.
41. M. Su, W. Feng, T. Jiang, B. Guo, H. Wang, and C. Zheng, "Disturbance observer-based sliding mode control for dynamic performance enhancement and current-sensorless of buck/boost converter," *IET Power Electron.*, 14 (2021): 1421–1432.
42. Zellouma, Y. Bekakra, and H. Benbouhenni, "Robust synergetic-sliding mode-based backstepping control of induction motor with MRAS technique," *Energy Reports*, 10 (2023): 3665-3680.
43. Zellouma, Y. Bekakra, and H. Benbouhenni, "Field-oriented control based on parallel proportional–integral controllers of induction motor drive," *Energy Reports*, 9 (2023): 4846-4860.
44. R. Sharma, S. Sharma, and S. Tiwari, "Design optimization of solar PV water pumping system," *Materials Today: Proceedings*, 21, no. 3 (2020): 1673-1679.
45. Mudlapur, V. V. Ramana, R. V. Damodaran, V. P. Balasubramanian, and S. Mishra, "Effect of partial shading on PV-fed induction motor water pumping systems," *IEEE Transactions on Energy Conversion*, 34, no. 1 (2019): 1–1.
46. M. Eltamaly, "A novel musical chairs algorithm applied for MPPT of PV systems," *Renewable and Sustainable Energy Reviews*, 146 (2021): 111135.
47. Mudlapur, V. V. Ramana, R. V. Damodaran, V. P. Balasubramanian, and S. Mishra, "Effect of partial shading on PV-fed induction motor water pumping systems," *IEEE Transactions on Energy Conversion*, (2018): 1–1.
48. R. Rai, S. Shukla, and B. Singh, "Sensorless field-oriented SMCC-based integral sliding mode for solar PV-based induction motor drive for water pumping," *IEEE Transactions on Industry Applications*, 56, no. 5 (2020): 1–1.
49. P. Fernández-Bustamante, I. Calvo, E. Villar, and O. Barambones, "Centralized MPPT based on sliding mode control and XBee 900 MHz for PV systems," *International Journal of Electrical Power & Energy Systems*, 153 (2023): 109350.
50. R. Kumar and B. Singh, "Grid interactive solar PV-based water pumping using BLDC motor drive," *IEEE Transactions on Industry Applications*, 55, no. 5 (2019): 1–1.
51. P. Guo, Y. Li, Z. Lin, Y. Li, and P. Su, "Characterization and calculation of losses in soft magnetic composites for motors with SVPWM excitation," *Applied Energy*, 349 (2023): 1–1.

52. Bhaumik and S. Das, "Virtual voltage vector-based predictive current control of speed sensorless induction motor drives," *ISA Transactions*, 133 (2023): 495-504.
53. M. Errouha and A. Derouich, "Study and comparison results of the field-oriented control for photovoltaic water pumping system applied on two cities in Morocco," *Bull. Electr. Eng. Informatics*, 8, no. 4 (2019): 1–7.
54. P. Kumar and I. Srikanth, "Power quality performance enhancement by PV-based distribution static compensator under incremental conductance maximum power point tracking algorithm," *Cleaner Energy Systems*, 4 (2023): 100062.
55. Y. Shtessel, M. Taleb, and F. Plestan, "A novel adaptive-gain supertwisting sliding mode controller: Methodology and application," *Automatica*, 48, no. 5 (2012): 759-769.
56. R. Benadli, D. Frey, Y. Lembeye, M. Bjaoui, B. Khiari, and A. Sellami, "A direct backstepping super-twisting algorithm controller MPPT for a standalone photovoltaic storage system: Design and real-time implementation," *J. Sol. Energy Eng.*, 145, no. 6 (2023): 061002.
57. M. Louzazni, H. Mosalam, and A. Khouya, "A non-linear auto-regressive exogenous method to forecast the photovoltaic power output," *Sustainable Energy Technologies and Assessments*, 38 (2020): 100670.
58. Chanda, P. Jana, and J. Das, "A tool to predict the evolution of phase and Young's modulus in high entropy alloys using artificial neural network," *Computational Materials Science*, 197 (2021): 110619.
59. De Ramón-Fernández, M. J. Salar-García, D. R. Fernández, J. Greenman, and I. Ieropoulos, "Evaluation of artificial neural network algorithms for predicting the effect of the urine flow rate on the power performance of microbial fuel cells," *Energy*, (2020): 118806.
60. Y. Ren, R. Wang, S. J. Rind, P. Zeng, and L. Jiang, "Speed sensorless nonlinear adaptive control of induction motor using combined speed and perturbation observer," *Control Engineering Practice*, 123 (2022): 105166.
61. M. Jouili, K. Jarray, Y. Koubaa, and M. Boussak, "Luenberger state observer for speed sensorless ISFOC induction motor drives," *Electric Power Systems Research*, 89 (2012): 139-147.
62. M. H. Holakooie, M. Ojaghi, and A. Taheri, "Full-order Luenberger observer based on fuzzy-logic control for sensorless field-oriented control of a single-sided linear induction motor," *ISA Transactions*, 60 (2016): 96-108.
63. Y. Zhang, Z. Yin, Y. Zhang, J. Liu, and X. Tong, "A novel sliding mode observer with optimized constant rate reaching law for sensorless control of induction motor," *IEEE Transactions on Industrial Electronics*, 67, no. 7 (2020): 1–1.
64. S. Carneiro, L. J. R. Silva, F. A. Faria, R. F. Q. Magossi, and V. A. Oliveira, "Reconfiguration strategy for a DC-DC boost converter using sliding mode observers and fault identification with a neural network," *Brazilian Society of Automation (SBA) - XV Brazilian Symposium on Intelligent Automation - SBAI 2021*, (2021): 1–1.
65. Zellouma, Y. Bekakra, and H. Benbouhenni, "Field-oriented control based on parallel proportional–integral controllers of induction motor drive," *Energy Reports*, 9 (2023): 4846-4860.
66. H. Vardhan, B. Akin, and H. Jin, "A low-cost, high-fidelity processor-in-the-loop platform: For rapid prototyping of power electronics circuits and motor drives," *IEEE Power Electronics Magazine*, 3, no. 2 (2016): 18-28.
67. A. Iqbal and G. K. Singh, "Closed loop operation and testing with processor-in-loop (PIL) simulation of an asymmetrical six-phase open-ended winding synchronous machine," *Journal of Engineering Research*, (2024): 12, no. 3, 433-443.
68. J. Zhang et al., "22.6 ANP-I: A 28nm 1.5pJ/SOP asynchronous spiking neural network processor enabling sub-O.1 μJ/sample on-chip learning for edge-AI applications," *2023 IEEE International Solid-State Circuits Conference (ISSCC)*, (2023): 21-23.
69. W. Sun et al., "MSONoC: A metasurface-assisted hybrid waveguide/FSO network-on-chip architecture," *IEEE Transactions on Green Communications and Networking*, (2024): 1–1.

70. A. Messai, A. Mellit, Guessoum, and S. Kalogirou, "Maximum power point tracking using a GA optimized fuzzy logic controller and its FPGA implementation," *Solar Energy*, 85, no. 2 (2011): 265–277.
71. H. Zheng, K. Wang, and A. Louri, "Adapt-NoC: A flexible network-on-chip design for heterogeneous manycore architectures," *2021 IEEE International Symposium on High-Performance Computer Architecture (HPCA)*, (2021): 723-735.
72. A. Kumar, V. K. Sehgal, G. Dhiman et al., "Mobile networks-on-chip mapping algorithms for optimization of latency and energy consumption," *Mobile Netw Appl*, 27 (2022): 637–651.
73. S. Biglari, F. Hosseini, A. Upadhyay, and H. Zhao, "Survey of network-on-chip (NoC) for heterogeneous multicore systems," *2024 IEEE 17th International Symposium on Embedded Multicore/Many-core Systems-on-Chip (MCSoC)*, (2024): 155-162.
74. H. Zheng, K. Wang, and A. Louri, "Adapt-NoC: A flexible network-on-chip design for heterogeneous manycore architectures," *2021 IEEE International Symposium on High-Performance Computer Architecture (HPCA)*, (2021): 723-735.